

Strongly Quenched Kramers Doublet Magnetism in $\text{SmMgAl}_{11}\text{O}_{19}$

Sonu Kumar,^{1, 2,*} Barbora Salajová,¹ Andrej Kancko,¹ Cinthia A. Corrêa,³ Shuvajit Halder,¹ and Ross H. Colman^{1, †}

¹*Charles University, Faculty of Mathematics and Physics,
Department of Condensed Matter Physics, Prague, Czech Republic*

²*Adam Mickiewicz University, Faculty of Physics and Astronomy,
Department of Experimental Physics of Condensed Phase, Poznań, Poland*

³*Institute of Physics of the Czech Academy of Sciences, Na Slovance, Prague, Czech Republic*

(Dated: January 21, 2026)

We report magnetic susceptibility, isothermal magnetization, and specific-heat measurements on the rare-earth hexaaluminate $\text{SmMgAl}_{11}\text{O}_{19}$, where Sm^{3+} realizes a strongly quenched Kramers doublet on a triangular lattice with an exceptionally weak net exchange scale. The Curie–Weiss analysis yields strongly reduced ground-doublet g factors, $g_{ab} \simeq 0.65$ and $g_c \simeq 0.70$. This indicates that the low-temperature response is governed primarily by single-ion physics, with crystal-field splitting and J -multiplet mixing jointly renormalizing the Sm^{3+} moment, rather than collective exchange. For $H \parallel c$, the specific heat shows no λ -type anomaly down to 0.35 K but evolves into a well-defined two-level Schottky peak whose gap grows linearly with field, yielding $g_c \simeq 0.62$ and recovering nearly all of $R \ln 2$ at high fields, thereby confirming an effective $S_{\text{eff}} = \frac{1}{2}$ Kramers doublet description for $T \lesssim 10$ K. Together, these results establish $\text{SmMgAl}_{11}\text{O}_{19}$ as a weak-exchange, nearly single-ion triangular Kramers magnet in which frustration produce an anisotropic low-field correlated regime without inducing long-range order.

I. INTRODUCTION

Frustrated magnetism provides a fertile route to emergent quantum states that cannot be captured by conventional mean-field ordering paradigms. In frustrated lattices, competing interactions or lattice geometry prevent spins from simultaneously satisfying all local constraints, leading to a macroscopic degeneracy of low-energy configurations and strongly suppressed ordering temperatures. When combined with low spin, strong spin–orbit coupling, or reduced dimensionality, geometric frustration suppresses conventional magnetic ordering tendencies, thereby allowing quantum fluctuations to dominate and potentially stabilize unconventional ground states such as quantum spin liquids (QSLs), spin glasses, and multipolar or topological phases. [1–4]. Identifying real materials that realize these regimes, and disentangling the role of disorder and single-ion physics, remains a central challenge in modern condensed-matter research.

Among the simplest geometries supporting strong frustration is the triangular-lattice antiferromagnet (TLAF). The TLAF has long served as a canonical platform for exploring correlation-driven physics, but it has gained renewed prominence in the last decade due to reports of QSL-like behavior in rare-earth TLAFs, most notably the triangular Yb-based insulator YbMgGaO_4 [5–9]. Although subsequent work has emphasized the importance of structural disorder in that compound, the broader impact was to establish rare-earth TLAFs as an experimentally accessible family where crystal-electric-field (CEF) ground-state doublets, strong spin–orbit coupling, and frustration cooperate to produce highly renormalized

ground states [10, 11]. This momentum has driven extensive searches for QSL and related phenomena across other frustrated lattices, including kagome systems such as herbertsmithite, kapellasite and Zn-barlowite [12–16], and pyrochlore magnets hosting spin-ice, quantum spin-ice, and spin-liquid regimes [17–25].

Rare-earth magnetoplumbite hexaaluminates $\text{LnMgAl}_{11}\text{O}_{19}$ constitute a particularly attractive but still emerging class of frustrated magnets. They crystallize in a centrosymmetric hexagonal magnetoplumbite structure, seen in figure 1, in which Ln^{3+} ions form quasi-two-dimensional triangular layers separated by nonmagnetic $\text{Al}/\text{Mg}–\text{O}$ blocks, so that antiferromagnetic interactions are expected to be strongest within each Ln layer and comparatively weak couplings acting between the layers, i.e., the system realizes a set of isolated triangular-lattice antiferromagnetic planes [26, 27]. The rare-earth layers host strongly spin–orbit-coupled local moments whose low-energy physics is governed by CEF-split Kramers or non-Kramers doublets due to the anisotropic ligand environments. As a result, this family spans distinct quantum limits: Kramers ions (e.g., Ce^{3+} , Nd^{3+}) can realize exchange-anisotropic effective spin- $\frac{1}{2}$ magnets, whereas non-Kramers ions (e.g., Pr^{3+}) allow additional multipolar degrees of freedom and enhanced coupling between spin and lattice [28–30]. Recent studies of Ce- and Pr-based hexaaluminates already point to exotic low-temperature behavior without long-range order, including strong single-ion anisotropy, pronounced CEF renormalization, and field-tunable thermodynamic anomalies [28, 29, 31–36], underscoring the potential of this platform for frustration-driven quantum magnetism.

Sm-based quantum magnets are, more broadly, well known as promising candidates for quantum-disordered ground states. The Sm^{3+} ion carries a small free-ion moment, strong Van Vleck susceptibility, and CEF exci-

* sonu.kumar@matfyz.cuni.cz

† ross.colman@matfyz.cuni.cz

tations. The low moment ensures weak exchange interactions, amplifying the importance of quantum fluctuations of an $S_{\text{eff}} = \frac{1}{2}$ ground-state doublet and rendering magnetic order unusually fragile [37–39]. In $\text{SmTa}_7\text{O}_{19}$ the frustrated lattice and these ingredients have been linked to persistent spin dynamics and QSL-like phenomenology [39]. A closely related scenario has recently been identified in the Nd analogues: the triangular-lattice hexaaluminate $\text{NdMgAl}_{11}\text{O}_{19}$ exhibits a magnetic ground state that closely mirrors that of $\text{NdTa}_7\text{O}_{19}$, with strong frustration and the absence of long-range order down to the lowest measured temperatures [30, 40]. This one-to-one correspondence between hexaaluminate and tantalate compounds suggests that $\text{SmMgAl}_{11}\text{O}_{19}$ may realize $\text{SmTa}_7\text{O}_{19}$ -like correlated or QSL-like behavior within the magnetoplumbite structure. Despite this motivation, a detailed single-crystal study of the Sm hexaaluminate $\text{SmMgAl}_{11}\text{O}_{19}$ has so far been missing, leaving its intrinsic anisotropy, thermodynamic ground state, and field response largely unexplored.

In this article we present a comprehensive structural, magnetic, and thermodynamic study of single-crystalline $\text{SmMgAl}_{11}\text{O}_{19}$. Using single-crystal X-ray diffraction, magnetometry, and field-dependent specific heat down to sub-Kelvin temperatures, we establish the quenched Kramers-doublet character of Sm^{3+} on a triangular lattice and quantify the extremely weak exchange scale. The combined data reveal a low-field correlated regime without long-range order down to the lowest measured temperatures and a crossover under field to a nearly ideal Zeeman-split doublet response. These results position $\text{SmMgAl}_{11}\text{O}_{19}$ as a key member of the rare-earth hexaaluminate family and a useful platform for studying how frustration, crystal-field excitations, and admixture of the $J = 7/2$ multiplet renormalize local doublet magnetism.

II. METHODS

The synthesis and subsequent crystal growth of $\text{SmMgAl}_{11}\text{O}_{19}$ were carried out using a conventional solid-state reaction followed by the optical floating-zone (OFZ) method. Initial precursor binary oxides (Sm_2O_3 , MgO , and Al_2O_3 , all 99.99% purity) were calcined at 800 °C for 24 h to remove moisture and carbonate contamination. The oxides were then weighed in the stoichiometric ratio, thoroughly mixed, and ground to ensure homogeneity of the mixture. The resulting powder was pressed into cylindrical rods with a 6 mm diameter and a length of about 100 mm. Densification was achieved using a quasihydrostatic pressure of 2 tons for 15 min, after which the rods were sintered in air at 1200 °C for 72 h to promote the solid-state reaction and improve the density.

Single crystals of $\text{SmMgAl}_{11}\text{O}_{19}$ were then grown in a four-mirror OFZ furnace under an air atmosphere with a slight overpressure of 1 atm and an air flow rate of

3 L/min. The sintered rods were used both as feed and seed material. During growth, the feed and seed rods were counter-rotated at 30 rpm to enhance temperature homogeneity and mixing in the molten zone, and the growth rate was maintained at 2 mm/h.

The single-crystalline nature of the resulting pieces was confirmed using backscattered Laue X-ray diffraction. A single-crystal X-ray diffraction (SCXRD) experiment was performed at 100 K on a XtaLAB Synergy R, DW system four-circle diffractometer, using a Mo rotating-anode X-ray tube (Mo $\text{K}\alpha$: $\lambda = 0.71073 \text{ \AA}$) with a mirror monochromator, and a hybrid pixel array detector HyPix-Arc 150°. Diffraction data were integrated using CrysAlis Pro [41] with an empirical absorption correction using spherical harmonics [42] combined with an analytical numeric absorption correction using a multifaceted crystal model implemented in the SCALE3 ABSPACK scaling algorithm. The structure was solved by charge flipping using the program Superflip [43] and refined by full-matrix least squares on F^2 in Jana2020 [44].

DC magnetic susceptibility measurements were carried out using a Quantum Design SQUID Magnetic Property Measurement System (MPMS3). Specific heat was measured from room temperature down to 0.35 K using a Quantum Design Physical Property Measurement System (PPMS9). Multiple pieces of single crystals were used for the bulk measurements; the consistency of the results confirms the sample quality and reproducibility. The data shown here were obtained from crystal pieces with masses of 7.8 mg, 4.72 mg, and 1.48 mg.

To isolate the magnetic contribution to the specific heat, non-magnetic $\text{LaMgAl}_{11}\text{O}_{19}$ single crystals were also grown in air by the floating-zone method and measured under identical conditions. A small low-temperature upturn in the $\text{LaMgAl}_{11}\text{O}_{19}$ specific heat indicates a tiny concentration of magnetic impurities; therefore, in the low-temperature limit ($T < 1 \text{ K}$) the phononic background used for subtraction was taken from a T^3 extrapolation of the measured $\text{LaMgAl}_{11}\text{O}_{19}$ heat capacity. The magnetic specific heat of $\text{SmMgAl}_{11}\text{O}_{19}$ was then obtained as $C_m(T) = C_{\text{Sm}}(T) - C_{\text{La}}^{\text{ph}}(T)$.

III. RESULTS

A. Structural characterization

The crystal structure of $\text{SmMgAl}_{11}\text{O}_{19}$ obtained by SCXRD at 100 K is hexagonal, space group $P6_3/mmc$ (#194), $Z = 2$, and with unit cell parameters $a = 5.57895(8) \text{ \AA}$ and $c = 21.8172(3) \text{ \AA}$, in line with the expected magnetoplumbite structure. Due to the identical electronic configuration of Mg^{2+} and Al^{3+} and, therefore, very similar X-ray atomic scattering factors, it is practically impossible to distinguish the site of Mg^{2+} ions site via SCXRD. Therefore, an initial model of $\text{SmAl}_{12}\text{O}_{19}$ was assumed, giving $\text{GOF} = 7.56\%$ and R_{obs}

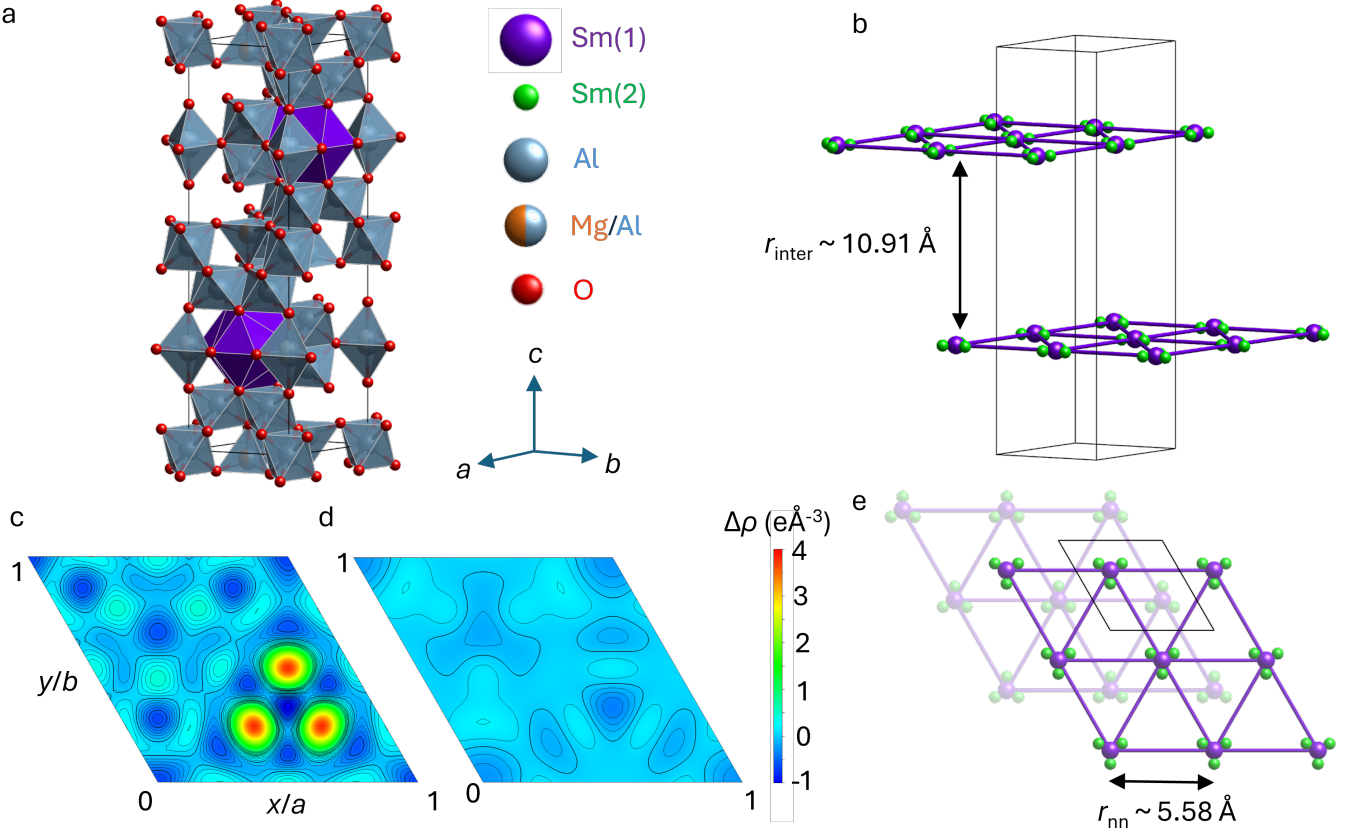


FIG. 1. (a) Magnetoplumbite structure of $\text{Sm}_{0.941}\text{MgAl}_{11}\text{O}_{19}$, with highlighted AlO_5 bipyramids and SmO_{12} polyhedra. (b) Triangular layers of Sm^{3+} ions, vertically separated by $r_{\text{inter}} = c/2 \approx 10.91 \text{ \AA}$. Fourier difference map projection at $z/c = 0.25$, showing the electronic density difference (c) before and (d) after the inclusion of the off-centered $\text{Sm}(2)$ ions on the $6h$ site. (e) Triangular lattice of $\text{Sm}(1)$ and $\text{Sm}(2)$ ions projected along the c axis, with the $\text{Sm}(1)$ - $\text{Sm}(1)$ distance $r_{\text{nn}} = 5.58 \text{ \AA}$.

$= 6.01\%$. Allowing the $\text{Sm}(1)$ occupancy to refine led to a noticeable improvement of the model, with $\text{occ}(\text{Sm}1) = 0.902(6)$, $\text{GOF} = 6.47\%$, and $R_{\text{obs}} = 5.54\%$, indicating a $\sim 10\%$ Sm^{3+} deficiency. Neutron diffraction experiments on the isostructural $\text{CeMgAl}_{11}\text{O}_{19}$ [36] suggest that Mg^{2+} is shared with Al^{3+} on the $\text{Al}(4)$ site. Splitting the $\text{Al}(4)$ site between Mg and Al with fixed 0.5/0.5 occupancies, with harmonic ADPs and coordinates constrained to be equal, the quality of the refinement practically stays unchanged - $\text{GOF} = 6.49\%$ and $R_{\text{obs}} = 5.53\%$. Individually placing the Mg ion on each of the remaining Al sites did not lead to an improvement of the model. In the magnetoplumbite structure, the $\text{Al}(5)$ ion is often distributed between two off-centered positions in the oxygen bipyramid, with the z -coordinate refined to $z(\text{Al}5) = 0.2434(4)$, resulting in the off-centering distance $\delta = 2(0.25 - z(\text{Al}5))c = 0.29 \text{ \AA}$. As was found previously, a significant improvement of the model was reached by adding a $\text{Sm}(2)$ atom to the $6h$ site at a distance of 0.855 \AA from $\text{Sm}(1)$ located on the $2d$ site [8]. Inspection of the Fourier difference maps in the ab -

plane cut at $z/c = 0.25$ (figures 1c and d) indicates a partially occupied atomic site (density 3.49 e\AA^{-3} and charge $1.41 e$). Inclusion of this positionally disordered (off-centered) $\text{Sm}(2)$ ion results in a substantial improvement of the agreement factors and yields $\text{GOF} = 2.63\%$ and $R_{\text{obs}} = 2.85\%$, and refined occupancies $\text{occ}(\text{Sm}1) = 0.862(2)$ and $\text{occ}(\text{Sm}2) = 0.0264(8)$. This solution gives the final formula $\text{Sm}_{0.941}\text{MgAl}_{11}\text{O}_{19}$, suggesting a $\sim 6\%$ total Sm^{3+} deficiency. A final improvement to the model was reached by employing an isotropic Becker-Coppens (Type 1, Gaussian) extinction parameter $G_{\text{iso}} = 0.244(14)$, leading to the final agreement factors $\text{GOF} = 2.06\%$ and $R_{\text{obs}} = 1.82\%$.

B. Magnetometry

Magnetic susceptibility data were first analyzed over the temperature range 1.8–100 K [Fig. 2]. In both orientations, $\chi^{-1}(T)$ exhibits strong curvature and no extended linear Curie–Weiss (CW) regime, indicating a

TABLE I. Summary of SCXRD structure solution results.

Chemical composition Sm _{0.941} MgAl ₁₁ O ₁₉	Crystal system, space group hexagonal, <i>P</i> 6 ₃ / <i>mmc</i> (#194) <i>Z</i> = 2	<i>a</i> = 5.57895(8) Å <i>c</i> = 21.8172(3) Å <i>V</i> = 588.078(14) Å ³	Crystal size 155x92x25 μm ³	Density (calculated) 4.3295 g.cm ⁻³								
X-ray tube: Mo K α (λ = 0.71073 Å) <i>T</i> = 99.9(2) K	No. of reflections measured/independent/observed 20883/695/638 Parameters refined: 49	Final <i>R</i> indices <i>R</i> _{obs} = 1.82% <i>wR</i> ₂ = 5.69% GOF = 2.0634	$\Delta\rho_{max}$, $\Delta\rho_{min}$ (eÅ ⁻³) 0.23, -0.38	Absorption μ = 5.733 mm ⁻¹								
Atom	Site Symm.	<i>x</i>	<i>y</i>	<i>z</i>								
Occ.		<i>U</i> ₁₁	<i>U</i> ₂₂	<i>U</i> ₃₃	<i>U</i> ₁₂	<i>U</i> ₁₃	<i>U</i> ₂₃	<i>U</i> _{eq}				
Sm(1)	2d -6m2	$\frac{1}{3}$	$\frac{2}{3}$	$\frac{3}{4}$	0.862(2)	108(1)	<i>U</i> ₁₁	39(1)	$\frac{1}{2}U_{11}$	0	0	85(1)
Sm(2)	6h <i>mm</i> 2	0.7413(6)	0.4826(6)	$\frac{1}{4}$	0.0264(8)	41(15)	<i>U</i> ₁₁	19(16)	-41(13)	0	0	61(12)
Al(1)	2a -3m.	0	0	0	1	29(3)	<i>U</i> ₁₁	37(4)	$\frac{1}{2}U_{11}$	0	0	32(2)
Al(2)	4f 3m.	$\frac{1}{3}$	$\frac{2}{3}$	0.19026(4)	1	34(2)	<i>U</i> ₁₁	32(3)	$\frac{1}{2}U_{11}$	0	0	33(2)
Al(3)	12k .m.	0.16755(7)	0.33509(4)	0.60869(2)	1	36(2)	36(2)	40(2)	$\frac{1}{2}U_{11}$	1(1)	$\frac{1}{2}U_{13}$	37(2)
Al(4)	4f 3m.	$\frac{1}{3}$	$\frac{2}{3}$	0.02740(4)	0.5	23(2)	<i>U</i> ₁₁	34(4)	$\frac{1}{2}U_{11}$	0	0	26(2)
Mg(1)	4f 3m.	$\frac{1}{3}$	$\frac{2}{3}$	0.02740(4)	0.5	23(2)	<i>U</i> ₁₁	34(4)	$\frac{1}{2}U_{11}$	0	0	26(2)
Al(5)	4e 3m.	0	0	0.2424(4)	0.5	49(3)	<i>U</i> ₁₁	120(30)	$\frac{1}{2}U_{11}$	0	0	72(11)
O(1)	6h <i>mm</i> 2	0.18177(14)	0.36335(3)	$\frac{1}{4}$	1	49(6)	115(5)	49(6)	$\frac{1}{2}U_{11}$	0	0	78(4)
O(2)	4e 3m.	0	0	0.15163(8)	1	23(9)	<i>U</i> ₁₁	50(16)	$\frac{1}{2}U_{11}$	0	0	47(3)
O(3)	12k .m.	0.1526(1)	0.3052(2)	0.05381(5)	1	56(3)	<i>U</i> ₁₁	54(4)	17(4)	9(2)	- <i>U</i> ₁₃	60(3)
O(4)	12k .m.	0.50585(10)	0.01170(10)	0.15208(4)	1	36(3)	<i>U</i> ₁₁	63(4)	15(3)	-4(1)	- <i>U</i> ₁₃	46(3)
O(5)	4f 3m.	$\frac{1}{3}$	$\frac{2}{3}$	0.55856(9)	1	33(4)	<i>U</i> ₁₁	74(8)	$\frac{1}{2}U_{11}$	0	0	47(4)

substantial temperature-independent Van Vleck contribution from virtual admixture with low-lying electronic excited states, as is typical of Sm-compounds [39, 45]. Nevertheless, fitting the data using a Curie–Weiss expression with temperature-independent terms,

$$\chi(T) = \frac{C}{T - \Theta_{CW}} + \chi_0, \quad (1)$$

yields consistently small Weiss temperatures in both orientations, confirming an extremely weak mean-field exchange interactions (Fig. 2b). For $H \parallel ab$, we obtain $\theta_{CW}^{ab} = 0.15(6)$ K and $\mu_{eff,ab} = 0.51 \mu_B$. For $H \parallel c$, the corresponding fit gives $\theta_{CW}^c = 0.68(1)$ K and $\mu_{eff,c} = 0.59 \mu_B$. Interpreting these as moments of an effective $S_{eff} = \frac{1}{2}$ doublet, using $\mu_{eff} = g\sqrt{S_{eff}(S_{eff}+1)} \mu_B = g\frac{\sqrt{3}}{2} \mu_B$, yields ground-state g factors $g_{ab} \simeq 0.59$ and $g_c \simeq 0.68$. These small effective moments and enhanced g factors, which differ markedly from the $^6H_{\frac{5}{2}}$ ground-multiplet free-ion expectations for Sm³⁺ ($g_J = 2/7$ and $\mu_{eff} = g_J\sqrt{J(J+1)} \approx 0.85 \mu_B$), highlight the importance of virtual mixing with the low-lying excited J -multiplet in renormalising the ground-state magnetic properties [46].

A more reliable description of the magnetic response is obtained by restricting the fit to the low-temperature regime, where only the ground-state Kramers doublet is expected to be thermally populated (Fig. 2c). For $H \parallel ab$, a Curie–Weiss fit including a temperature-independent term, $\chi(T) = C/(T - \Theta_{CW}) + \chi_0$, between 1.8 and 9.5 K yields $\theta_{CW}^{ab} = 0.08(8)$ K, $\mu_{eff,ab} = 0.56(2) \mu_B$, and $\chi_0^{ab} = 2.21 \times 10^{-4}$ emu/mol. For $H \parallel c$, the corresponding fit gives $\theta_{CW}^c = 2.8(1.9) \times 10^{-4}$ K, $\mu_{eff,c} = 0.60(2) \mu_B$, and a markedly larger background

$\chi_0^c = 1.56 \times 10^{-3}$ emu/mol. Interpreting these effective moments in terms of an $S_{eff} = \frac{1}{2}$ doublet yields ground-state g factors $g_{ab} \simeq 0.65$ and $g_c \simeq 0.70$.

The reduced effective moments and the strong anisotropy of χ_{vv} are consistent with a Kramers doublet ground state whose magnetic response is strongly renormalised by inter-multiplet (J -mixing) effects, leading to moderate axial anisotropy and extremely weak effective exchange interactions.

Isothermal magnetization measurements reveal a pronounced but unsaturated response at low temperature in both field orientations (Fig. 3). At 1.8 K, $M(H)$ shows clear curvature (sublinear increase with field) and reaches $M_c \approx 0.24 \mu_B/\text{Sm}$ for $H \parallel c$ and $M_{ab} \approx 0.19 \mu_B/\text{Sm}$ for $H \parallel ab$ at the highest applied field, without any sign of saturation. Upon warming to 3 K and 5 K, the overall magnetization is reduced across the full field range. By 10 K the magnetization becomes essentially linear in both directions and the anisotropy between $H \parallel c$ and $H \parallel ab$ is strongly diminished.

To quantify the low-energy response in terms of an effective Kramers doublet, we fit $M(H)$ using a modified spin- $\frac{1}{2}$ Brillouin form,

$$M(H) = M_{sat} \tanh(x) + \chi_0 \mu_0 H, \quad (2)$$

$$x = \frac{g \mu_B \mu_0 H}{2k_B T}, \quad (3)$$

where g is the effective g factor of the ground doublet and $M_{sat} = N_A g \mu_B / 2$ for one effective spin- $\frac{1}{2}$ per Sm. In both orientations, agreement with Eqs. (2) and (3) becomes apparent only for $T \geq 5$ K, while clear systematic deviations persist at 1.8 K and 3 K (more pronounced for $H \parallel ab$). Fitting the data for $H \parallel c$

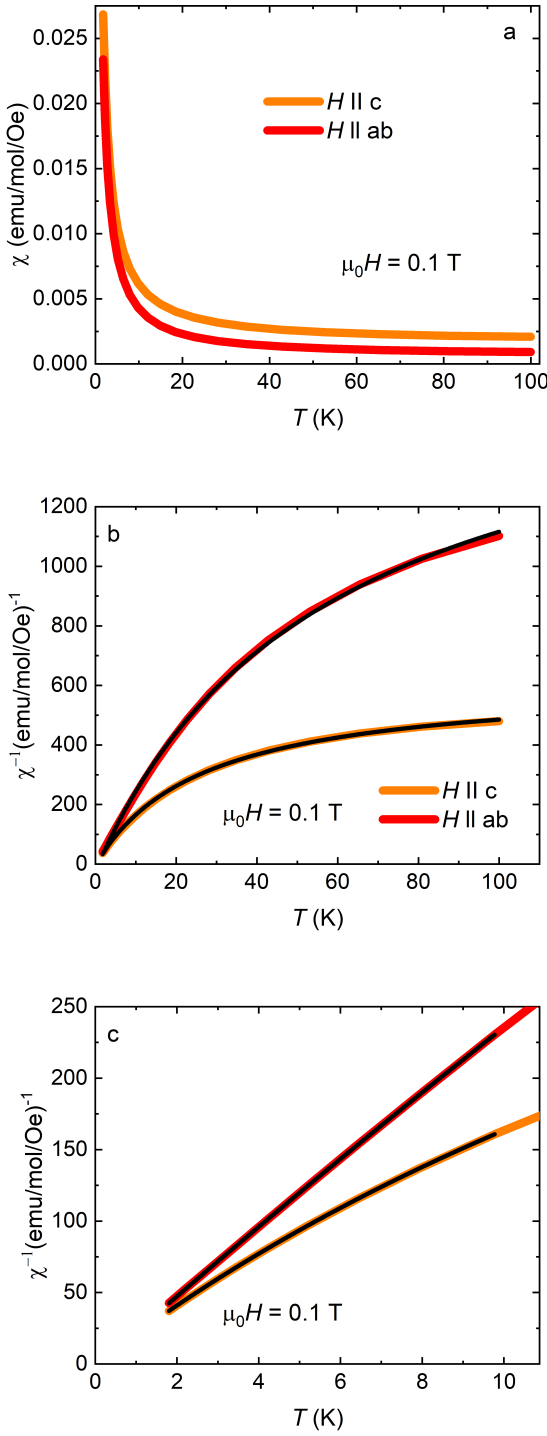


FIG. 2. (a) DC magnetic susceptibility $\chi(T)$ of $\text{SmMgAl}_{11}\text{O}_{19}$ for $H \parallel c$ and $H \parallel ab$ measured in an applied field of $\mu_0 H = 0.1 \text{ T}$. (b) Inverse susceptibility $1/\chi(T)$ for both field directions over the full temperature range, together with Curie–Weiss fits including a Van Vleck term (solid black lines). (c) Low-temperature inverse susceptibility for $H \parallel c$ and $H \parallel ab$ in the 1.8–10 K range, highlighting the linear CW+ χ_{vv} behavior in the ab plane and its absence along c . Solid black lines show the corresponding CW+ χ_{vv} fits.

yields $g_c = 0.65213(36)$ and $\chi_{0,c} = 2.14(2) \times 10^{-3}$, whereas for $H \parallel ab$ we obtain $g_{ab} = 0.57628(69)$ and $\chi_{0,ab} = 7.31(33) \times 10^{-4}$.

The breakdown at the lowest temperatures is consistent with additional low-energy contributions beyond an isolated two-level description. The temperature-independent background extracted from $M(H)$ fits is of the same order as that obtained from Curie–Weiss analysis of $\chi(T)$, with modest differences likely reflecting the distinct sensitivity of the two protocols to field-linear contributions and weak non-idealities (e.g., internal-field distributions and fitting-window dependence).

C. Crystal electric field calculations

To quantify the single-ion anisotropy of Sm^{3+} in $\text{SmMgAl}_{11}\text{O}_{19}$, we performed CEF calculations using the PyCRYSTALFIELD package [47] and the refined crystallographic structure. Sm^{3+} occupies a unique rare-earth site in the magnetoplumbite lattice and is coordinated by twelve oxygen ligands forming a distorted SmO_{12} polyhedron with approximate trigonal symmetry. The local axes were chosen as $z \parallel c$ and $y \parallel a$, and the ligand environment was truncated at $r \leq 3 \text{ \AA}$, which captures the twelve nearest oxygen ions. To avoid ambiguity from crystallographic multiplicity, we explicitly selected the $\text{Sm}(1)$ site (occupancy 1) when constructing the local environment. The twelve oxygen ligands form two closely spaced radial shells at $d \simeq 2.641 \text{ \AA}$ and 2.793 \AA .

As a baseline electrostatic estimate we adopted a purely ionic point-charge model in which the oxygen ligands were assigned $q_O = -2e$ while all non-oxygen neighbors were taken as neutral. The resulting single-ion Hamiltonian can be expressed in Stevens-operator form,

$$\mathcal{H}_{\text{CEF}} = \sum_{n,m} B_m^n O_m^n, \quad (4)$$

where O_m^n are Stevens operators and B_m^n are the CEF parameters. With the above axis choice and the near-trigonal ligand geometry, the point-charge solution yields the dominant trigonal terms (B_2^0, B_4^0, B_6^0 , and B_6^6), while the remaining coefficients are negligible within numerical precision.

A CEF description restricted to a single J multiplet can be incomplete for Sm^{3+} because the temperature-independent susceptibility is often dominated by virtual excitations and intermultiplet (“ J -mixing”) processes. We therefore diagonalized the single-ion problem in the intermediate-coupling (LS-mixed) basis implemented in PYCRYSTALFIELD. In this framework, the parameter `LS_Coupling` controls the degree of multiplet mixing and provides a phenomenological way to include intermultiplet contributions, which are well documented in Sm^{3+} magnetism (see, e.g., Ref. [48]). In our analysis, we used the experimentally determined Van Vleck susceptibility as an empirical constraint to optimize the multiplet-mixing strength in the point-charge model and

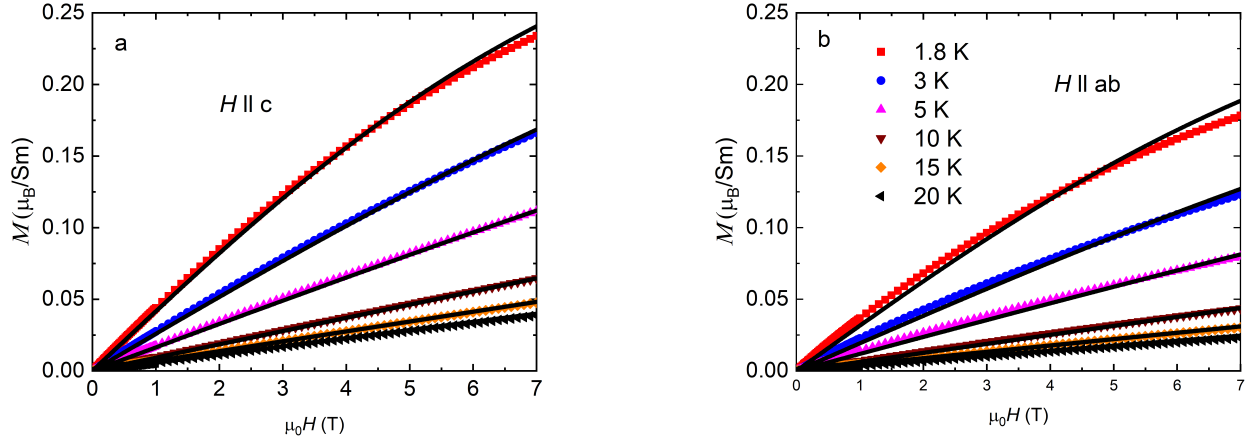


FIG. 3. (a) Isothermal magnetization $M(H)$ of $\text{SmMgAl}_{11}\text{O}_{19}$ for $H \parallel c$ at several temperatures. (b) Isothermal magnetization $M(H)$ for $H \parallel ab$. Both panels show the weak anisotropy and absence of saturation up to 7 T.

thereby renormalize the low-energy response into quantitative agreement with experiment. The results quoted below correspond to LS_Coupling= 17 meV (for the justification for this value, see Discussion).

Within this LS-mixed ionic point-charge model, the low-energy CEF spectrum consists of a Kramers doublet ground state followed by excited doublets at $\Delta_1 = 7.34$ meV and $\Delta_2 = 25.01$ meV (relative to the ground doublet), with the next levels above ~ 60 meV. These higher-lying states are not thermally populated at low temperature but contribute to the response through virtual excitations (Van Vleck channel).

The ground-doublet g tensor in the chosen local frame is nearly diagonal but contains a small xz mixing,

$$\mathbf{g} = \begin{pmatrix} 0.509 & 0 & 0.330 \\ 0 & 0.607 & 0 \\ 0.381 & 0 & 0.587 \end{pmatrix}.$$

corresponding to principal values $(g_1, g_2, g_3) \approx (0.607, 0.607, 0.700)$. Identifying the principal axis closest to the crystallographic c direction as g_c yields $g_{ab} \simeq 0.6$ and $g_c \simeq 0.7$, in excellent agreement with the $g \approx 0.6$ –0.7 values extracted from low-temperature magnetometry.

We emphasize that the calculation is still based on an ionic point-charge description and therefore does not explicitly include covalency or screening, so a spectroscopic determination of the CEF levels is ultimately required for a confident assignment.

Nevertheless, for Sm^{3+} the dominant correction to a single- J description arises from intermultiplet admixture, which is naturally captured by the LS-mixed framework. By calibrating the degree of multiplet mixing using the experimental Van Vleck contribution, our optimized point-charge model achieves quantitative agreement with the experimentally inferred g tensor and supports an ef-

fective pseudospin- $\frac{1}{2}$ Kramers doublet below ~ 10 K, with the next CEF excitations on energy scales far above the exchange scale inferred from thermodynamic measurements.

D. Specific heat and magnetic entropy

The specific-heat data provide a complementary thermodynamic perspective on the low-energy physics of $\text{SmMgAl}_{11}\text{O}_{19}$. In zero field, the magnetic specific heat $C_m(T)$ shows no λ -type anomaly down to 0.35 K, excluding conventional long-range magnetic order within our experimental window (Fig. 4a). Instead, $C_m(T)$ exhibits a low-temperature upturn with a weak kink-like feature. Given the absence of any corresponding anomaly in susceptibility or magnetization, these low-temperature features are most naturally attributed to a combination of nuclear Schottky contributions from Sm isotopes and minor impurity- or defect-related effects.

Applying a magnetic field drives the system toward a regime dominated by single-ion physics. For fields of 2–7 T, $C_m(T)$ develops a pronounced Schottky-like peak that shifts systematically to higher temperature with increasing field, as expected for a Zeeman-split Kramers doublet (Fig. 4a). These anomalies are well described by a simple two-level Schottky form

$$C_{\text{Sch}} = f R \left(\frac{\Delta}{T} \right)^2 \frac{\exp[-\Delta/T]}{\left[1 + \exp(-\Delta/T) \right]^2}, \quad (5)$$

where R is the molar gas constant, Δ is the field-dependent energy gap of the effective Kramers doublet, and f is an effective filling fraction that accounts for the reduced number of active Sm moments. The gaps extracted from these high-field anomalies increase linearly with field and correspond to an out-of-plane effective

$g_c \simeq 0.62$, in excellent agreement with the magnetization-based estimates. At lower fields, the evolution of the Schottky anomaly reveals the emergence of a regime where magnetic correlations play a more significant role in the low temperature properties. When the field is reduced below ~ 3 T, the peak amplitude of the hump is markedly suppressed, in contrast to the field-independent peak height expected for an ideal two-level non interacting Schottky anomaly with fixed entropy (Fig. 4a). In the language of the Schottky fits, this corresponds to a progressive reduction of the effective filling fraction f with decreasing field, with f dropping particularly strongly already at $\mu_0 H = 1$ T (Fig. 4c). Such amplitude loss implies that only a subset of Sm^{3+} ions experiences a well-defined Zeeman gap at low fields, while the remaining moments contribute to a broad distribution of low-energy configurations shaped by weak exchange, dipolar interactions, and disorder on the frustrated triangular lattice. This interpretation is consistent with the sizable residual entropy that persists down to the base temperature at low and zero field, and with the anisotropic magnetic response inferred from susceptibility and magnetization. The field dependence of the entropy further underscores this picture: only in sufficiently strong fields does the system fully unlock the doublet degrees of freedom, with the magnetic entropy approaching the full $R \ln 2$ between 0.35 and 10 K by $\mu_0 H \approx 5$ T (Fig. 3b). At the same time, Despite the Curie–Weiss temperatures remaining very close to zero, the Schottky fits reveal a strong suppression of the effective filling fraction f as the field is reduced, indicating that a substantial fraction of Sm^{3+} moments is effectively quenched rather than simply exchange-decoupled. This is fully compatible with the reduced effective moment extracted from magnetization and with the sizable Van Vleck contributions to the susceptibility in both field directions. Taken together, the thermodynamic data establish a crossover from a low-field correlated regime with entropy locked in low-energy modes to a high-field single-ion regime governed by a Zeeman-split Kramers doublet.

IV. DISCUSSION

The magnetometry of $\text{SmMgAl}_{11}\text{O}_{19}$ places the material in the weak-exchange limit of a rare-earth triangular-lattice magnet in which single-ion physics dominates, yet the consequences of weak residual interactions remain experimentally visible. Curie–Weiss analysis yields Weiss temperatures that are essentially zero in both orientations, demonstrating that the net exchange scale is extremely small. Using a mean-field estimate for a triangular lattice ($z = 6$) with an effective $S = \frac{1}{2}$ doublet, the magnitude of a nearest-neighbor exchange compatible with such tiny Θ_{CW} is on the order of $|J|/k_B \lesssim 0.05$ K, i.e., far below typical crystal-field and Zeeman energy scales. In this regime, geometric frustration, together with the $\sim 6\%$ Sm-site deficiency, can efficiently can-

cel and randomize weak interactions, leaving the response governed primarily by a strongly quenched local Kramers doublet. At the same time, the absence of a sizable exchange scale means that even subtle disorder- or interaction-induced renormalizations remain visible in the low-temperature response.

Within this weak-exchange background, the low-temperature susceptibility reveals a clear directional contrast. In the ab plane, M/H is well described by a Curie law once the small, temperature-independent Van Vleck contribution is taken into account, and the slight sub-Curie trend in the raw M/H mainly reflects this additive χ_{vv}^{ab} . Consistent with an almost single-ion Kramers doublet, the isothermal magnetization for $H \parallel ab$ collapses onto an approximately universal curve when plotted as M against H/T (Fig. 5b), as expected for a paramagnet with a single dominant energy scale set by the Zeeman splitting. For both field directions, the corrected inverse susceptibility $(\chi - \chi_0)^{-1}$ is nearly linear between 1.8 and 10 K, showing that in this low-temperature window the response is well captured by a Curie term from an effective doublet plus a temperature-independent background (Fig. 6a). Interpreting the effective moments in terms of an $S_{\text{eff}} = \frac{1}{2}$ doublet yields ground-state g factors $g_{ab} \simeq 0.65$ and $g_c \simeq 0.70$, reduced compared to the free-ion Sm^{3+} value and already indicating strong quenching of the local moment.

When the same analysis is extended to higher temperatures, clear deviations from this simple picture emerge. Extending $(\chi - \chi_0)^{-1}$ up to 100 K, we find that for $H \parallel ab$ the corrected inverse susceptibility bends away from linearity already above $T \sim 20$ K, while for $H \parallel c$ a noticeable deviation sets in above $T \sim 80$ K (Fig. 6b). This demonstrates that the quenching of the Sm^{3+} moment cannot be attributed to a single mechanism such as a rigid, isolated CEF doublet with a fixed g tensor. Instead, it reflects a combination of crystal-field splitting within the $J = 5/2$ manifold, admixture of the excited $J = 7/2$ multiplet, and weak residual interactions and disorder, whose relative importance grows as thermally populated excited states contribute to the response.

To quantify the role of J -multiplet mixing, we interpret the Van Vleck term in the standard J -mixing framework for Sm^{3+} [49]. In this approach the temperature-independent susceptibility is written as

$$\chi_{\text{vv}} = \frac{N_A \mu_B^2}{k_B} \alpha_J, \quad (6)$$

with

$$\alpha_J = \frac{20}{7\Delta}, \quad (7)$$

where $\Delta = E_{J+1} - E_J$ is the energy separation (in kelvin) between the excited ($J = \frac{7}{2}$) and ground ($J = \frac{5}{2}$) multiplets of Sm^{3+} . Using the cgs conversion

$$\frac{N_A \mu_B^2}{k_B} \simeq 0.375 \text{ emu K/mol},$$

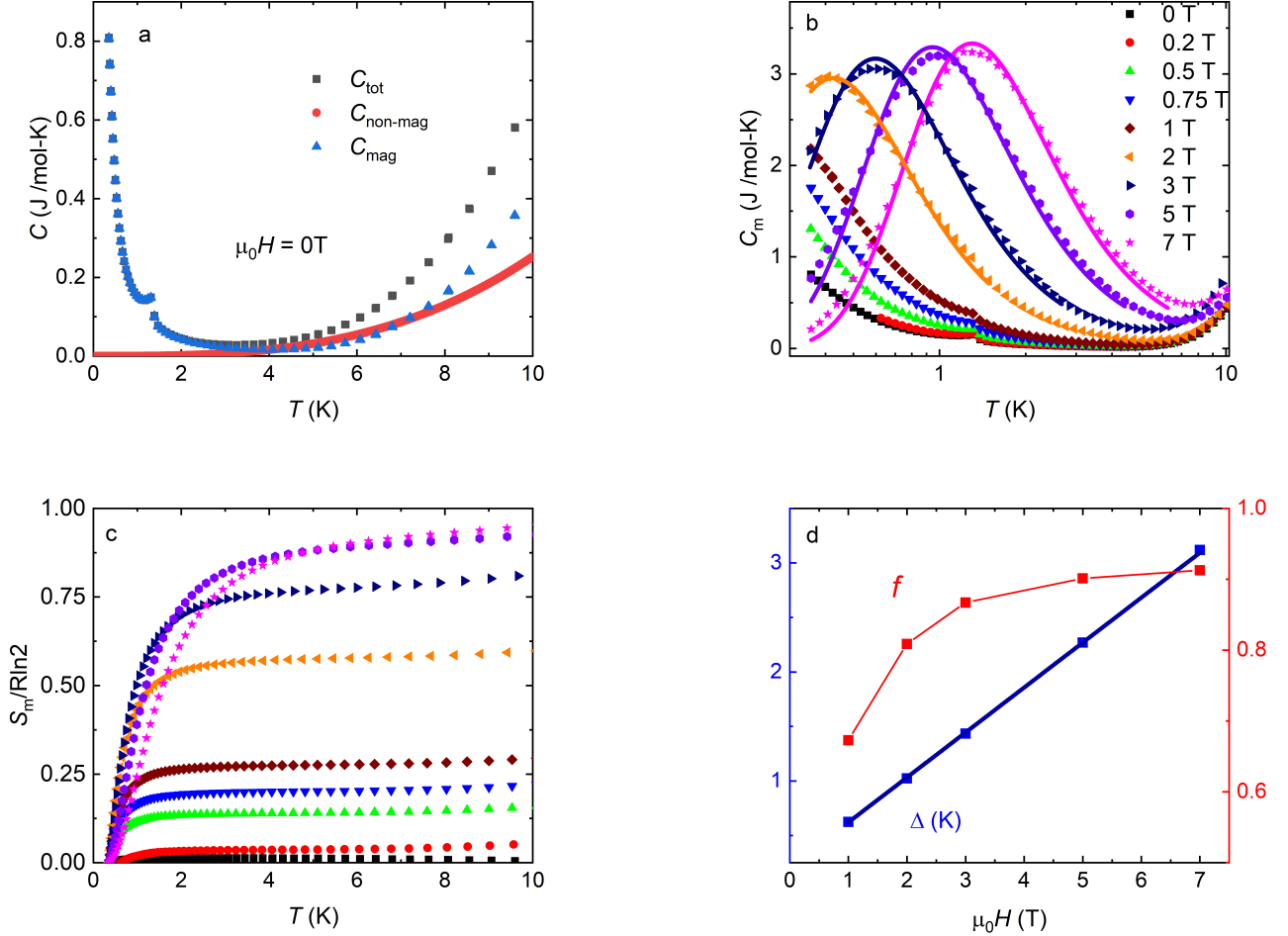


FIG. 4. **Fig. 3.** Specific heat and Schottky analysis of SmMgAl₁₁O₁₉. (a) Total specific heat $C_p(T)$ of SmMgAl₁₁O₁₉ together with the nonmagnetic analogue LaMgAl₁₁O₁₉, and the magnetic contribution $C_m(T)$ extracted by subtracting the phonon background in zero field. (b) Magnetic specific heat $C_m(T)$ of SmMgAl₁₁O₁₉ under various applied magnetic fields. Solid curves show two-level Schottky fits for $\mu_0 H \geq 1$ T. (c) Magnetic entropy $S_m(T)$ obtained from integrating C_m/T . (d) Zeeman gap $\Delta(B)$ and filling fraction $f(B)$ extracted from the Schottky analysis. The solid blue line represents a linear fit to $\Delta(B)$.

and our low-temperature fit for $H \parallel c$, $\chi_{vv}^c = 1.56 \times 10^{-3}$ emu/mol, we obtain

$$\alpha_J^{(c)} = \frac{\chi_{vv}^c}{N_A \mu_B^2 / k_B} = \frac{1.56 \times 10^{-3}}{0.375} \simeq 4.2 \times 10^{-3} \text{ K}^{-1},$$

and hence an effective multiplet gap

$$\Delta_{\text{eff}} = \frac{20}{7 \alpha_J^{(c)}} \simeq 6.8 \times 10^2 \text{ K.}$$

Expressed in energy units, this corresponds to

$$\Delta_{\text{eff}} \simeq \frac{6.8 \times 10^2 \text{ K}}{11.6045 \text{ K/meV}} \simeq 59 \text{ meV.}$$

To connect this estimate to the intermediate-coupling calculations, we relate the $J = \frac{5}{2} \rightarrow \frac{7}{2}$ separation to

the effective spin-orbit (LS) coupling constant ζ via the Russell-Saunders expression

$$E_J = \frac{\zeta}{2} [J(J+1) - L(L+1) - S(S+1)], \quad (8)$$

with $L = 5$ and $S = \frac{5}{2}$ for the 6H_J term of Sm³⁺. This gives

$$\Delta_{7/2-5/2} = E_{7/2} - E_{5/2} = \frac{7}{2} \zeta, \quad (9)$$

and therefore

$$\zeta_{\text{eff}} = \frac{2}{7} \Delta_{\text{eff}} \simeq \frac{2}{7} \times 59 \text{ meV} \simeq 16.9 \text{ meV.}$$

This value provides a quantitative basis for the multiplet-mixing parameter used in PYCRYSTALFIELD: we set LS_Coupling ≈ 17 meV in the CEF calculations so that

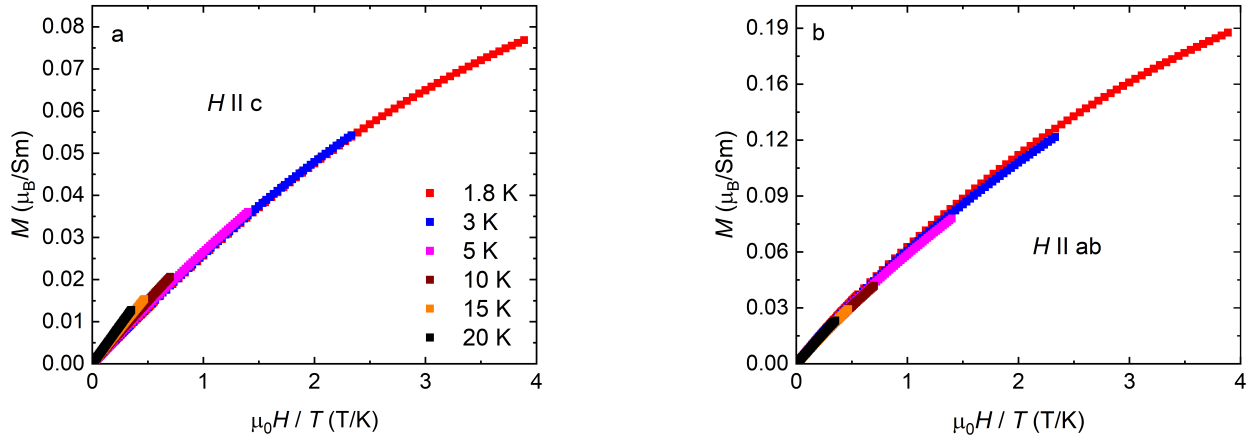


FIG. 5. (a) Scaling plot of magnetization for $\text{SmMgAl}_{11}\text{O}_{19}$ with magnetization M plotted against H/T for fields applied along the c axis. The absence of scaling collapse indicates the presence of additional low-energy correlations and internal fields for $H \parallel c$. (b) Scaling of M vs. H/T for $H \parallel ab$. The near-universal collapse of the curves is consistent with predominantly single-ion paramagnetic behavior in the ab plane.

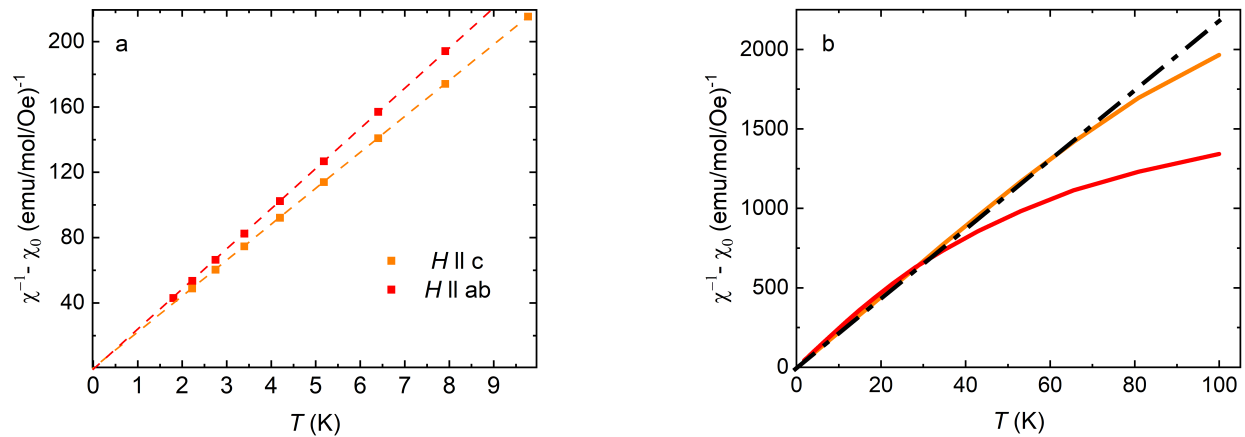


FIG. 6. (a) Inverse corrected susceptibility $(\chi - \chi_0)^{-1}$ as a function of temperature in the low-temperature window $1.8 \leq T \leq 10$ K, showing a nearly linear Curie-Weiss behaviour of the ground-state Kramers doublet. (b) $(\chi - \chi_0)^{-1}$ over the extended temperature range, highlighting the breakdown of simple Curie-Weiss scaling.

the degree of intermultiplet admixture is consistent with the Van Vleck response extracted from $\chi(T)$.

This effective $J = \frac{5}{2} \rightarrow \frac{7}{2}$ separation is somewhat smaller than the free-ion spin-orbit splitting expected for Sm^{3+} , as anticipated since part of the observed Van Vleck response also originates from CEF mixing within the $J = \frac{5}{2}$ manifold and from higher J multiplets. We therefore interpret Δ_{eff} as a lower bound on the true multiplet gap and as a quantitative measure that J -multiplet mixing makes a substantial contribution to the quenching of the Sm^{3+} moment in $\text{SmMgAl}_{11}\text{O}_{19}$.

The isothermal magnetization provides complementary insight. Even after including a linear $\chi_0 H$ term, an effective spin- $\frac{1}{2}$ Brillouin form does not reproduce

$M(H)$ quantitatively at the lowest temperatures. This mismatch is physically informative rather than a fitting artifact: a Brillouin+Van Vleck model assumes a uniform two-level system with a single g tensor and no distribution of local environments. In $\text{SmMgAl}_{11}\text{O}_{19}$, several effects naturally violate this idealization. Weak frustrated interactions can still renormalize the low- T field response even when $\Theta_{\text{CW}} \approx 0$; Sm-site deficiency and local disorder broaden the CEF landscape and thus generate a spread of effective g factors and internal fields; and the proximity of excited CEF levels enables additional field-induced mixing beyond a strict two-level description. The improvement of Brillouin-like behavior at intermediate temperatures is then consistent with ther-

mal suppression of the weakest disorder- and interaction-induced effects, whereas deviations re-emerge upon further heating as excited CEF states become thermally populated.

The thermodynamic data provide a crucial and fully consistent perspective on these magnetic trends. Specific-heat measurements were performed with $H \parallel c$ only, because the crystals cleave very strongly in the ab plane, resulting in thin platelets that are difficult to mount with the field perpendicular to the c axis. Along the c axis, the zero- and low-field regime shows no ordering anomaly down to the base temperature and releases only a small fraction of the doublet entropy. At low fields, a Schottky-like anomaly develops, but with a noticeably reduced peak amplitude compared to the high-field limit, indicating that only a subset of Sm^{3+} ions contributes to a well-defined Zeeman-split two-level response, while the remaining spectral weight is tied up in low-energy configurations that do not behave as an ideal Schottky doublet. In other words, the system is not fully polarized in fields below about 5 T, and a finite fraction of the doublet entropy remains locked in weakly interacting or disordered degrees of freedom. This picture is consistent with the low-temperature deviations of $M(H)$ from a simple Brillouin form and explains why a single effective gap cannot describe the magnetization in the weak-field regime.

Upon increasing the field along c , the system crosses over into a high-field single-ion regime dominated by a Zeeman-split Kramers doublet. The Schottky anomaly becomes well defined, its gap grows linearly with field, and the integrated entropy approaches the doublet value of $0.94 R \ln 2$, demonstrating that strong fields suppress internal-field distributions and residual correlations, thereby restoring an almost ideal two-level response. The nearly vanishing Curie-Weiss temperatures and the reduced effective g factor ($g_c \simeq 0.6$) show that this response is governed primarily by a strongly quenched Sm^{3+} doublet and its Zeeman splitting, rather than by a sizable exchange gap. The concurrent improvement of magnetization scaling and the approach toward Brillouin-like behaviour in the same field range further confirm the crossover from a correlated low-field regime with partially locked entropy to a polarized single-ion regime dominated by Zeeman physics of a renormalized doublet.

At higher temperatures, irrespective of field direction, the response crosses over into a CEF-mixed paramagnetic regime where excited crystal-field levels contribute strongly. This is reflected in the curvature of $\chi^{-1}(T)$ outside the low-temperature Curie-Weiss window and in the re-emergence of non-Brillouin behaviour in $M(H)$ above a few kelvin. Thus, within the measured range the overall behaviour is governed not by sharp phase boundaries but by two crossovers: (i) a field-driven crossover along c from a low-field correlated doublet regime with reduced filling fraction f to a high-field Zeeman single-ion regime where most of the doublet entropy is released, and (ii) a thermal crossover out of the ground-doublet manifold into

a CEF-mixed paramagnet. While the specific-heat data constrain the T - B diagram quantitatively only for $H \parallel c$, the magnetometry indicates that the ab -plane channel remains closer to the single-ion limit over a broader temperature range, consistent with its smaller Van Vleck contribution and more robust scaling collapse.

It is instructive to contrast $\text{SmMgAl}_{11}\text{O}_{19}$ with the recently reported $\text{SmTa}_7\text{O}_{19}$, as both materials host Sm^{3+} Kramers ions on triangular lattices with strong spin-orbit coupling and CEF-split effective $J_{\text{eff}} = 1/2$ ground states. In $\text{SmTa}_7\text{O}_{19}$, sizeable antiferromagnetic exchange [$\Theta_{\text{CW}} \sim -0.4$ to -0.7 K in both orientations] together with strong geometric frustration places the system in a regime where collective dynamics dominate: zero- and longitudinal-field μSR reveal persistent low-temperature spin fluctuations, the specific heat exhibits a $\log T$ contribution together with a characteristic $C_m \propto T^2$ power law at high fields, and the overall thermodynamic response is consistent with a gapless, QSL-like state [39].

By contrast, $\text{SmMgAl}_{11}\text{O}_{19}$ realizes the extreme weak-exchange limit of a Sm-based triangular lattice. Here Θ_{CW}^{ab} is close to zero, the effective moment of the ground doublet is strongly reduced, and the high-field magnetization and Schottky anomaly are well captured by a strongly quenched single-ion Kramers doublet with a small effective g factor, renormalized by the combined effects of crystal-field splitting and J -multiplet mixing. At low fields, the Schottky peak becomes broadened and suppressed, and the doublet entropy is only partially released within the experimental window, indicating a weak, anisotropic low-field regime that deviates from an ideal two-level Schottky response and likely reflects residual internal-field distributions and non-idealities, rather than a robust exchange-driven QSL state of the type realized in $\text{SmTa}_7\text{O}_{19}$.

For simplicity, all analyses were performed assuming one Sm per formula unit, although the refined composition is $\text{Sm}_{0.941}\text{MgAl}_{11}\text{O}_{19}$; therefore, the intrinsic magnetic response per Sm ion may be slightly larger.

Within the broader $\text{LnMgAl}_{11}\text{O}_{19}$ hexaaluminate family, $\text{SmMgAl}_{11}\text{O}_{19}$ thus occupies the most weakly interacting, single-ion-dominated limit of the phase diagram. $\text{CeMgAl}_{11}\text{O}_{19}$ hosts an XXZ-anisotropic Kramers doublet tuned close to a quantum critical point [28], while $\text{NdMgAl}_{11}\text{O}_{19}$ exhibits strong single-ion anisotropy and frustration that suppress long-range order down to 45 mK [30]. The non-Kramers compound $\text{PrMgAl}_{11}\text{O}_{19}$, by contrast, shows a split quasi-doublet and induced quantum-Ising-like dynamics with much larger moment and interaction scales [29]. In this landscape, $\text{SmMgAl}_{11}\text{O}_{19}$ stands out as a strongly quenched, nearly single-ion reference point, in which the ground-state doublet is renormalized by both crystal-field effects and J -multiplet mixing, complementary to the exchange-dominated QSL-like regime exemplified by $\text{SmTa}_7\text{O}_{19}$ and to the more strongly interacting Kramers and non-Kramers hexaaluminates.

V. CONCLUSIONS

In summary, $\text{SmMgAl}_{11}\text{O}_{19}$ realizes a Sm^{3+} Kramers doublet on a triangular lattice with strongly quenched effective moment, in the extreme weak-exchange limit. Magnetometry and c -axis specific heat consistently point to a low-field correlated regime in which part of the doublet entropy remains locked in weakly interacting or disordered degrees of freedom, and the field response deviates from that of an ideal two-level system. Under applied field along c , the system crosses over into an almost single-ion regime governed by a Zeeman-split Kramers doublet with a strongly reduced effective g factor ($g_c \simeq 0.6$) and a nearly recovered doublet entropy. The modest anisotropy of the bulk response is best understood as arising from anisotropic matrix elements and Van Vleck contributions associated with crystal-field splitting and J -multiplet mixing, rather than from any large exchange anisotropy.

Looking ahead, local-probe μSR down to dilution temperatures can test for ultra-low- T freezing or persistent slow dynamics and quantify internal-field distributions in the correlated regime. Extending specific

heat and magnetization measurements into the dilution-refrigerator range will further constrain the fate of the residual entropy and the nature of the low-field correlations. More broadly, $\text{SmMgAl}_{11}\text{O}_{19}$ provides a nearly single-ion, strongly quenched reference point within the $\text{LnMgAl}_{11}\text{O}_{19}$ family, complementary to the more strongly interacting Kramers and non-Kramers members and to exchange-dominated Sm-based triangular magnets such as $\text{SmTa}_7\text{O}_{19}$.

ACKNOWLEDGMENTS

We acknowledge funding from Charles University in Prague within the Grant Agency of Univerzita Karlova (grant number 438425). The work was also supported by the Ministry of Education, Youth and Sports of the Czech Republic through program INTER-EXCELLENCE II INTER-ACTION (LUABA24056). Crystal growth, structural analysis, and magnetic properties measurements were carried out in the MGML (<http://mgml.eu/>), supported within the Czech Research Infrastructures program (project no. LM2023065). This work was further supported by the Grant Agency of the Czech Republic (grant number 26-23051S).

[1] L. Balents, *Nature* **464**, 199 (2010).
 [2] L. Savary and L. Balents, *Rep. Prog. Phys.* **80**, 016502 (2017).
 [3] C. Broholm, R. J. Cava, S. A. Kivelson, D. G. Nocera, M. R. Norman, and T. Senthil, *Science* **367**, eaay0668 (2020).
 [4] A. P. Ramirez and S. V. Syzranov, *Mater. Adv.* **6**, 1213 (2025).
 [5] Y. Li, H. Liao, Z. Zhang, S. Li, F. Jin, L. Ling, L. Zhang, Y. Zou, L. Pi, Z. Yang, J. Wang, Z. Wu, and Q. Zhang, *Sci. Rep.* **5**, 16419 (2015).
 [6] Y. Shen, Y.-D. Li, H. C. Walker, P. Steffens, M. Boehm, X. Zhang, S. Shen, H. Wo, G. Chen, and J. Zhao, *Nat. Commun.* **9**, 4138 (2018).
 [7] Y. Li, H. Liao, Z. Zhang, S. Li, F. Jin, L. Ling, L. Zhang, Y. Zou, L. Pi, Z. Yang, J. Wang, Z. Wu, and Q. Zhang, *Sci. Rep.* **5**, 16419 (2015).
 [8] Y. Li, D. Adroja, P. K. Biswas, P. J. Baker, Q. Zhang, J. Liu, A. A. Tsirlin, P. Gegenwart, and Q. Zhang, *Phys. Rev. Lett.* **117**, 097201 (2016).
 [9] X. Rao, G. Hussain, Q. Huang, W. J. Chu, N. Li, X. Zhao, Z. Dun, E. S. Choi, T. Asaba, L. Chen, L. Li, X. Y. Yue, N. N. Wang, J.-G. Cheng, Y. H. Gao, Y. Shen, J. Zhao, G. Chen, H. D. Zhou, and X. F. Sun, *Nat. Commun.* **12**, 4949 (2021).
 [10] Z. Zhu, P. A. Maksimov, S. R. White, and A. L. Chernyshev, *Phys. Rev. Lett.* **119**, 157201 (2017).
 [11] Y. Li, D. Adroja, R. I. Bewley, D. Voneshen, A. A. Tsirlin, P. Gegenwart, and Q. Zhang, *Phys. Rev. Lett.* **118**, 107202 (2017).
 [12] Y. Y. Huang, Y. Xu, L. Wang, C. C. Zhao, C. P. Tu, J. M. Ni, L. S. Wang, B. L. Pan, and Y. Fu, *Phys. Rev. Lett.* **127**, 267202 (2021).
 [13] M. R. Norman, *Rev. Mod. Phys.* **88**, 041002 (2016).
 [14] V. R. Shaginyan, K. G. Popov, and V. A. Khodel, *J. Exp. Theor. Phys.* **116**, 848 (2013).
 [15] R. W. Smaha, W. He, J. M. Jiang, J. Wen, Y.-F. Jiang, J. P. Scheckton, C. J. Titus, S. G. Wang, Y.-S. Chen, S. J. Teat, A. A. Aczel, Y. Zhao, G. Xu, J. W. Lynn, H.-C. Jiang, and Y. S. Lee, *npj Quantum Mater.* **5**, 23 (2020).
 [16] K. Tustain, B. Ward-O'Brien, F. Bert, T. Han, H. Luetkens, T. Lancaster, B. M. Huddart, P. J. Baker, and L. Clark, *npj Quantum Mater.* **5**, 74 (2020).
 [17] S. T. Bramwell and M. J. P. Gingras, *Science* **294**, 1495 (2001).
 [18] Y. Huang, K. Chen, Y. Deng, N. Prokof'ev, and B. Svistunov, *Phys. Rev. Lett.* **116**, 177203 (2016).
 [19] M. J. P. Gingras and P. A. McClarty, *Rep. Prog. Phys.* **77**, 056501 (2014).
 [20] X.-P. Yao, Y.-D. Li, and G. Chen, *Phys. Rev. Research* **2**, 013334 (2020).
 [21] T. An, F. Desrochers, and Y. B. Kim, *Phys. Rev. B* **112**, 195109 (2025).
 [22] J. E. Greedan, *J. Alloys Compd.* **408–412**, 444 (2006).
 [23] L. Savary, X. Wang, H.-Y. Kee, Y. B. Kim, Y. Yu, and G. Chen, *Phys. Rev. B* **94**, 075146 (2016).
 [24] F. Desrochers, L. E. Chern, and Y. B. Kim, *Phys. Rev. B* **105**, 035149 (2022).
 [25] D. R. Yahne, B. Placke, R. Schäfer, O. Benton, R. Moessner, M. Powell, J. W. Kolis, C. M. Pasco, A. F. May, M. D. Frontzek, E. M. Smith, B. D. Gaulin, S. Calder, and K. A. Ross, *Phys. Rev. X* **14**, 011005 (2024).
 [26] M. Gasperin, M. C. Saine, A. Kahn, F. Laville, and A. M.

Lejus, *J. Solid State Chem.* **54**, 61 (1984).

[27] D. Saber and A. M. Lejus, *Mater. Res. Bull.* **16**, 1325 (1981).

[28] G. Bastien, A. Eliáš, V. Anderle, A. Kancko, C. A. Corrêa, S. Kumar, P. Proschek, J. Prokleška, L. Nádherný, D. Sedmidubský, T. Treu, P. Gegenwart, M. Kratochvílová, M. Žonda, and R. H. Colman, arXiv preprint arXiv:2506.16207 (2025).

[29] S. Kumar, M. Klicpera, A. Eliáš, M. Kratochvílová, A. Kancko, C. Correa, K. Załęski, M. Śliwińska Bartkowiak, R. H. Colman, and G. Bastien, *Phys. Rev. B* **111**, 174444 (2025).

[30] S. Kumar, J. Prokleška, K. Załęski, A. Kancko, C. A. Correa, M. Śliwińska-Bartkowiak, G. Bastien, and R. H. Colman, arXiv e-prints , arXiv:2505.18898 (2025), arXiv:2505.18898 [cond-mat.str-el].

[31] Y. Cao, H. Bu, Z. Fu, J. Zhao, J. S. Gardner, Z. Ouyang, Z. Tian, Z. Li, and H. Guo, *Mater. Futures* **3**, 035201 (2024).

[32] N. Li, A. Rutherford, Y. Y. Wang, H. Liang, Q. J. Li, Z. J. Zhang, H. Wang, W. Xie, and H. D. Zhou, *Phys. Rev. B* **110**, 134401 (2024).

[33] Z. Ma, S. Zheng, Y. Chen, R. Xu, Z.-Y. Dong, J. Wang, H. Du, J. P. Embs, S. Li, Y. Li, Y. Zhang, M. Liu, R. Zhong, J.-M. Liu, and J. Wen, *Phys. Rev. B* **109**, 165143 (2024).

[34] C. P. Tu, Z. Ma, H. R. Wang, Y. H. Jiao, D. Z. Dai, and S. Y. Li, *Phys. Rev. Research* **6**, 043147 (2024).

[35] Y. Cao, A. Koda, M. D. Le, V. Pomjakushin, B. Liu, Z. Fu, Z. Li, J. Zhao, Z. Tian, and H. Guo, *Sci. China Phys. Mech. Astron.* **68**, 267011 (2025).

[36] B. Gao, T. Chen, C. Liu, M. L. Klemm, S. Zhang, Z. Ma, X. Xu, C. Won, G. T. McCandless, N. Murai, S. Ohira-Kawamura, S. J. Moxim, J. T. Ryan, X. Huang, X. Wang, J. Y. Chan, S.-W. Cheong, O. Tchernyshyov, L. Balents, and P. Dai, arXiv e-prints , arXiv:2408.15957 (2024), 10.48550/arXiv.2408.15957, arXiv:2408.15957 [cond-mat.str-el].

[37] M. B. Sanders, F. A. Cevallos, and R. J. Cava, *Mater. Res. Express* **4**, 036102 (2017).

[38] M. B. Sanders, K. M. Baroudi, J. W. Krizan, O. A. Mukadam, and R. J. Cava, arXiv preprint arXiv:1601.06639 (2016), 10.48550/arXiv.1601.06639.

[39] D. Bairwa, A. Bandyopadhyay, D. Adroja, G. B. G. Stenning, H. Luetkens, T. J. Hicken, J. A. Krieger, G. Cibin, M. Rotter, S. Rayaprol, P. D. Babu, and S. Elizabeth, *Phys. Rev. B* **111**, 104413 (2025).

[40] T. Arh, B. Sana, M. Pregelj, P. Khuntia, Z. Jagličić, M. D. Le, P. K. Biswas, P. Manuel, L. Mangin-Thro, A. Ozarowski, and A. Zorko, *Nat. Mater.* **21**, 416 (2022).

[41] Rigaku Oxford Diffraction, “CrysAlispro software, version 1.171.43.143a,” (2024), rigaku Oxford Diffraction.

[42] R. C. Clark and J. S. Reid, *Acta Crystallogr. Sect. A* **51**, 887 (1995).

[43] L. Palatinus and G. Chapuis, *J. Appl. Cryst.* **40**, 786 (2007).

[44] V. Petříček, L. Palatinus, J. Plášil, and M. Dušek, *Z. Kristallogr. Cryst. Mater.* **238**, 271 (2023).

[45] V. Peçanha-Antonio, E. Feng, X. Sun, D. Adroja, H. C. Walker, A. S. Gibbs, F. Orlandi, Y. Su, and T. Brückel, *Phys. Rev. B* **99**, 134415 (2019).

[46] A. Abragam and B. Bleaney, *Electron Paramagnetic Resonance of Transition Ions* (Oxford University Press, Oxford, 1970).

[47] A. Scheie, *J. Appl. Cryst.* **54**, 356 (2021).

[48] V. Peçanha-Antonio, E. Feng, X. Sun, D. Adroja, H. C. Walker, A. S. Gibbs, F. Orlandi, Y. Su, and T. Brückel, *Physical Review B* **99**, 134415 (2019).

[49] D. Wagner, *Introduction to the Theory of Magnetism*, International Series in Natural Philosophy, Vol. 48 (Pergamon Press, Oxford, 1972).